Electronic Communication through a Metal-Metal Quadruple Bond

Honors Research Thesis

Presented in partial fulfillment of the requirements for graduation *with honors research distinction* in Chemistry in the undergraduate colleges of The Ohio State University

by

Philip Bunting

The Ohio State University

June 2012

Project Advisor: Professor Malcolm H. Chisholm, Department of Chemistry

Abstract

Mixed valence compounds are incredibly useful tools for studying electron transfer. Most inorganic mixed valence compounds are of the form $[M\text{-}B\text{-}M]^{+}$, where M is a metal-based redox center and B is a chemical bridge (usually an organic ligand). Herein, we describe the synthesis and characterization of inorganic mixed valence compounds of the form $[L\text{-}M\text{-}L]^{-}$, where L is a ligand based redox center and electronic communication is facilitated through the metal center. The compounds are of the form $M_2(TiPB)_2(nic\text{-}B(C_6F_5)_3)_2$, where TiPB = 2,4,6-triisopropylbenzoate, nic = 4-isonicotinate, and M = Mo (**1B**) or W (**2B**). The electronic structures of **1B** and **2B** (and their parent compounds) are examined using electronic structure calculations and UV-vis spectroscopy. The characterization of the anions $\mathbf{1B}^{-}$ and $\mathbf{2B}^{-}$ allows us to assess the ability of the M_2 bridge to facilitate electron transfer between the two redox sites. The separation of reduction peaks in cyclic voltammetry ($\Delta E_{1/2}$ = 300 mV (**1B**) and 650 mV (**2B**)) suggests, as expected, that the tungsten center is better at coupling the redox centers. Additionally, the absorption peaks and band shapes associated with charge resonance (or IVCT) in the NIR ($\mathbf{1B}^{-}$ = 3800 cm^{-1}; $\mathbf{2B}^{-}$ = 4500 cm^{-1}) allow us to assign **1B** and **2B** to Class II/III and Class III mixed valence ions, respectively; while both compounds have fully delocalized charge, the coupling is larger for the tungsten compound.

1. Background on Electron-Transfer Reactions

1.1 Transition State Theory to Marcus Theory

Transition state theory describes the progression of a chemical reaction from reactants to products through an intervening transition state. The theory is best illustrated through the use of a potential energy diagram; where the energy of the reactants, products, and transition state is plotted against the reaction coordinate (**Figure 1.1**). The plot is a 2-dimensional reduction of the actual potential energy surface where the transition state is a saddle point between the two minima that represent the reactants and products. Transition state theory is incredibly useful for describing reactions (and their mechanisms) that have changes in structure and connectivity (e.g. S_N1, S_N2, E1, and E2 reactions) because each point on the potential energy diagram can be associated with a specific molecular geometry. For example, consider that in **Figure 1.1** the bond lengths in the transition state are between those of the reactants and products.

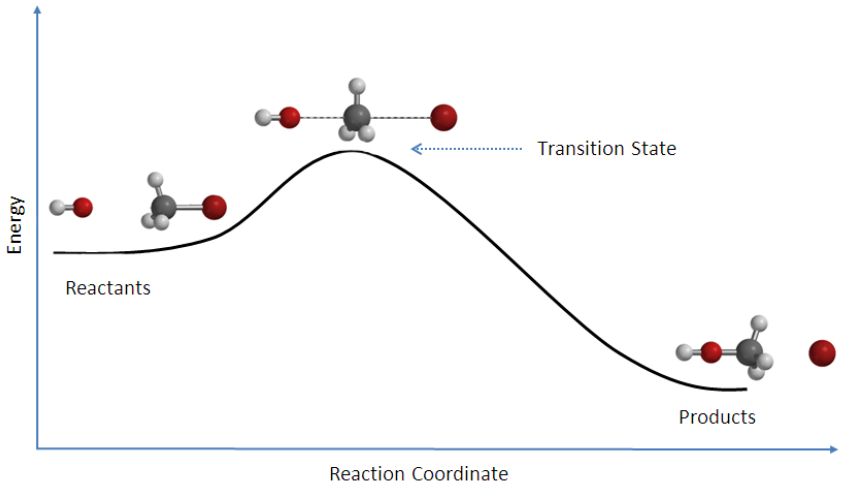

Figure 1.1. An example of a potential energy diagram that treats a reaction with transition state theory.

As stated above, the purpose of transition state theory is to give insight into the mechanisms of chemical reactions. All chemical reactions involve the movement of electrons,

but in the case of the chemical reactions suitable for treatment with this theory, they also involve movements of nuclei. If, however, we want to focus our attention on just the movement of electrons, we need to use a different type of reaction: an electron-transfer reaction.

Electron-transfer reactions involve the movement of an electron from a donor site to an acceptor site with no significant change in geometry; the major change in this reaction is simply the location of an electron. With regard to a reaction coordinate, the location of an electron cannot be tracked as a reactant is in transition state theory. Because an electron is an elementary particle, it is either on the donor or on the acceptor, and there is no intermediate transition state. Thus, to explain the mechanisms of electron-transfer reactions, we need a new theory.

Starting in 1956[1], Rudolph A. Marcus began to develop his theory on electron transfer, now known as Marcus Theory (for which he received a Nobel Prize in Chemistry in 1992). A brief overview follows.

1.2 Outer Sphere vs. Inner Sphere Electron Transfer

Before we look at the various treatments for electron transfer (ET) reactions, it is important to note the different types of ET reactions.

The inner coordination sphere refers to atoms, ions, or ligands directly connected to the central atom/ion. For example, the cyanide ligands in $[Fe(CN)_6]^{3-}$ are in the inner sphere. Relative to the outer coordination sphere, the ligands in the inner sphere are fixed with regard to positions and bond lengths. The outer coordination sphere refers to the surrounding solvent molecules. While there can be ideal locations and orientations for the outer sphere molecules, movement in the outer sphere is much more fluid and less predictable.

Outer sphere ET (which was the focus of Marcus's original work[1]) can be viewed as the transfer of charge between two hard spheres. These hard spheres float around in solution until they bump into each other, at which point, if the conditions are right, an electron may hop from the donor to acceptor.

Inner sphere ET (which is the focus of Marcus-Hush theory) occurs when the donor and acceptor are linked via a bridge. The bridge, which can be an atom or molecule and may be fixed or temporary, provides a pathway for the electron to travel from donor to acceptor.

Figure 1.2 illustrated the changes that occur in inner and outer spheres in an ET reaction. Note the changes in solvent orientation (outer sphere) and changes in radius (inner sphere)

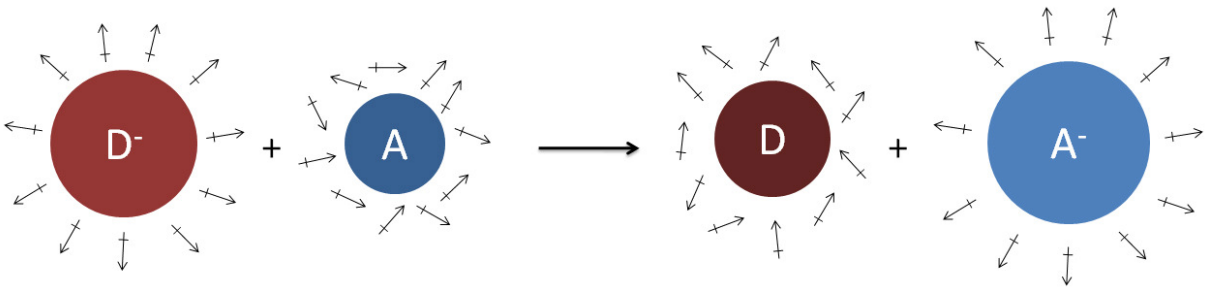

Figure 1.2. An illustration of an electron transfer reaction showing the changes in radii (inner sphere) and solvent orientation (outer sphere)

1.3 Marcus Theory: Outer Sphere, Diabatic Treatment

Consider an electron transfer reaction, where an electron hops from the donor, D, to the acceptor, A:

$$D^- + A \rightarrow D + A^- \qquad \textbf{(1.1)}$$

The potential energy of all participating compounds can be represented, using a harmonic oscillator approximation, with parabolas. If we further simplify by combining all parameters (bond lengths, angles, etc.) of D^- and A, we can draw one parabola, *r*, that represents the reactants, and another, *p*, which represents the products. Note that, for example, sitting at the bottom of the potential energy well *r* means that the electron is on the donor and the geometries and solvation spheres of D^- and A are optimized accordingly. The energy of these potential energy surfaces are plotted along the reaction coordinate, x. To track the progression of the reaction, we center *r* at x=0 and *p* at x=1. Also, if D and A are different compounds, the electron transfer will have an accompanying change in energy, ΔE_0. If, on the other hand, D and A are the same compounds, the reaction is termed "self-exchange" and $\Delta E_0=0$. The above considerations are summarized in Figure 1.3

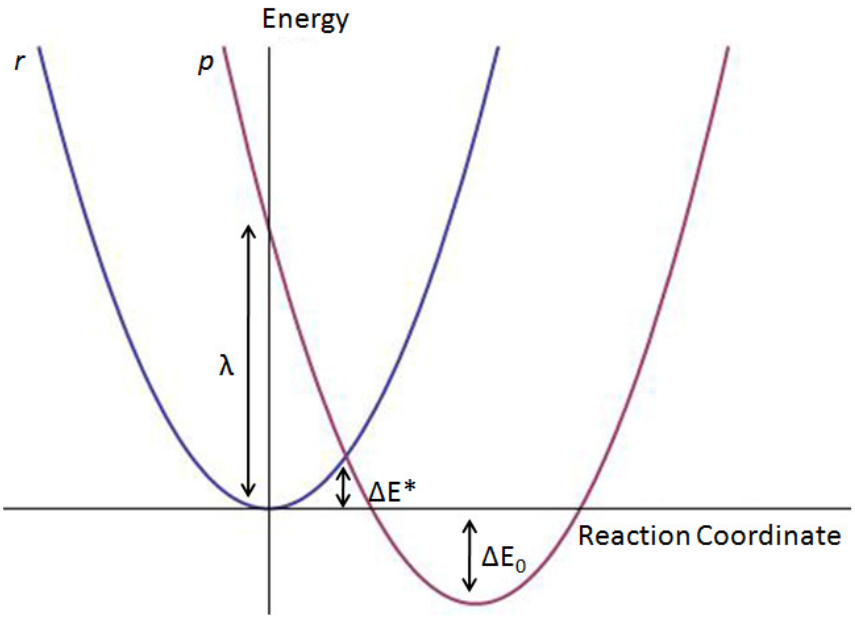

Figure 1.3. Diabatic potential energy curves for an electron transfer reaction. On curve *r*, the electron is on the donor; on *p* it is on the acceptor. λ is the reorganizational energy; ΔE_0 is the free energy release associated with the reaction; and ΔE^* is the energy requirement for thermal electron transfer.

Because we are working with harmonic oscillators, we can easily describe the system using the following equations:

$$r = \lambda \mathrm{x}^2 \tag{1.2}$$

$$p = \lambda(\mathrm{x} - 1)^2 + \Delta \mathrm{E}_0 \tag{1.3}$$

where λ (called the reorganizational energy) is the reduced forced constant (which applies to both reactants and products), and x is the displacement along the reaction coordinate. The point of interest, of course, is the intersection of the two parabolas. Some simple algebra gives us the nuclear coordinate of intersection, X*, and the energy at the intersection, E*:

$$X^* = \frac{1}{2}\left(1 + \frac{\Delta E_0}{\lambda}\right) \tag{1.4}$$

$$\Delta E^* = \frac{\lambda}{4}\left(1 + \frac{\Delta E_0}{\lambda}\right)^2 \tag{1.5}$$

Note that in the case of self-exchange, X^*=1/2 and ΔE^*=λ/4.

There are two ways for an electron to move from the *r* curve to the *p* curve: an optical and a thermal transfer. In an optical transition, an electron, which initially sits at the bottom of the *r* curve, absorbs an appropriate amount of light to move to the *p* curve directly above it. Because electron transfers are much faster than nuclear movement, the system is still at x=0, meaning the system is optimized for the electron to be on the donor when it is actually on the acceptor. The energy required to change the system (solvent orientation, etc.) is equal to λ, the reorganization energy. After adjustment, the system is at x=1 and on the *p* curve.

Regarding thermal electron transfer, consider that moving along a potential energy curve means making the parameters of the compounds (i.e. solvent orientation, bond lengths, etc.)

more or less appropriate for the state the electron is in. The solvation of the donor is drastically different at the beginning and end of the reaction (going from the *r* curve at x=0 to the *p* curve at x=1). However, we know that the movement of an electron is essentially instantaneous relative to the movement of the solvent molecules, so the solvent molecules cannot change orientation as the electron is moving. What is required, then, is for the solvent to begin to reorganize *before* the electron transfers. As this happens, the solvation will become less ideal, and the system will move along the *r* curve toward x=1, increasing in energy. When the system reaches X*, the solvation will look like a cross between the solvation spheres seen at x=0 and x=1; at this point, the environment will be not be ideal for the electron to be on either the donor or the acceptor. The additional energy required to make this non-ideal system (called the precursor complex) is equal to ΔE^*. At X* with energy ΔE^*, the electron can hop from donor to acceptor, and in the potential energy diagram we move from *r* to *p* curves. Once the electron is on the acceptor, the solvent molecules continue to reorganize until they reach a system represented by the *p* curve at x=1.

Note that there are several differences between this ET mechanism and the mechanisms suggested in transition state theory. Firstly, the precursor complex is one that simply meets an energy requirement, but there is no specific corresponding geometry (that is, many solvation sphere environments may meet the requirement). Also, although the solvent molecules must move gradually, the electron transfer is instantaneous.

The fact that this ET is outer sphere is reflected in the fact that (1) the *r* and *p* curves in Figure 1.3 are diabatic (they cross but do not interact) and (2) the process of ET is referred to as hopping. Once a precursor complex has formed, an electron transfer may or may not occur. The

probability of an electron transfer is given by the transmission coefficient, κ, which varies from 0 to 1.

Knowing the energy required to form the precursor complex (ΔE*) we can predict the rate of electron transfer, k_{et}, in the normal Arrhenius manner (where the probability of an ET and the collision frequency, v_n is placed in the pre-exponential factor):

$$k_{et} = \kappa v_N e^{\left(-\frac{\Delta E^*}{RT}\right)} \quad \textbf{(1.6)}$$

where R is the gas constant, and T is the absolute temperature of the system.

As with many good theories, Marcus Theory led to a prediction of an as then unseen phenomenon. Another look at Eq. 1.5 suggests that ΔE* is minimized (and rate is maximized) when the free energy of the reaction, ΔE_0, is equal to the opposite of the reorganization energy, λ. If the reaction becomes more exothermic**,** the rate actually begins to decrease (as shown in Figure 1.4). This phenomenon is referred to as the Marcus inverted region, and was experimentally proven in 1984[2].

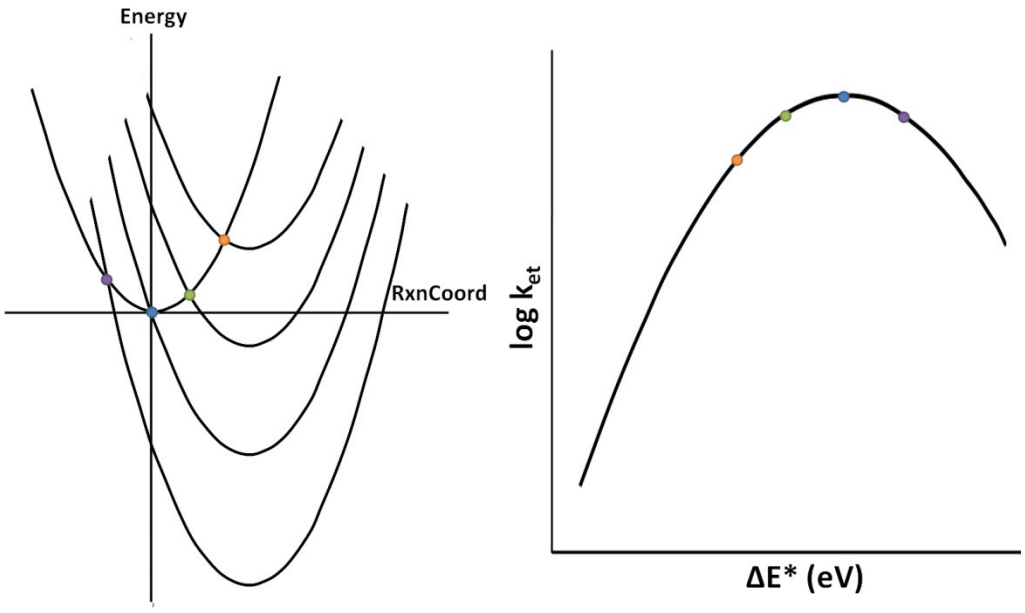

Figure 1.4. An illustration of the Marcus Inverted Region. The maximum rate is achieved when the reorganizational energy, λ, is equal to the opposite of the free energy of the reaction, ΔE_0.

1.4 Marcus-Hush: Inner sphere, Adiabatic treatment

So far we have considered electron transfer between non-interacting, diabatic potential energy curves that correspond to outer sphere ET. In reality, it is more likely that there is some interaction between the product and reactant curves. Physically, this interaction can manifest itself in the form of a chemical bridge that facilitates the electron transfer, making this type of ET inner sphere. This coupling of redox centers is reflected in the electronic coupling of wavefunctions; our original diabatic curves are coupled to form two new adiabatic curves. To obtain equations for these curves, we begin by solving the secular equation:

$$\begin{vmatrix} H_{AA} - E & H_{AB} \\ H_{AB} & H_{BB} - E \end{vmatrix} = 0 \qquad \textbf{(1.7)}$$

where $H_{AA} = \langle\psi_A|H|\psi_A\rangle$ is the energy of the system in its initial state (the system resides solely on the reactant curve), $H_{BB} = \langle\psi_B|H|\psi_B\rangle$ is the energy of the system in its final state (they system resides solely on the product curve), H is the Hamiltonian operator for the system, and $H_{AB} = \langle\psi_A|H|\psi_B\rangle$ is the electronic coupling matrix element. The roots of the Eq. 1.7 are[3]:

$$E_{\pm} = \frac{(H_{AA}+H_{BB})}{2} \mp \frac{[(H_{AA}-H_{BB})^2+4H_{AB}^2]^{\frac{1}{2}}}{2} \quad \textbf{(1.8)}$$

and if we let $H_{AA} = r = \lambda x^2$ and $H_{BB} = p = \lambda x^2 + \Delta E_0$, the adiabatic curves are expressed as[3]:

$$E_{\pm} = \frac{[\lambda(2x^2-2x+1)+\Delta E_0]}{2} \mp \frac{[[\lambda(2x-1)+\Delta E_0]^2+4H_{AB}^2]^{\frac{1}{2}}}{2} \quad \textbf{(1.9)}$$

These curves, along with their original diabatic curves, are shown in Figure 1.5.

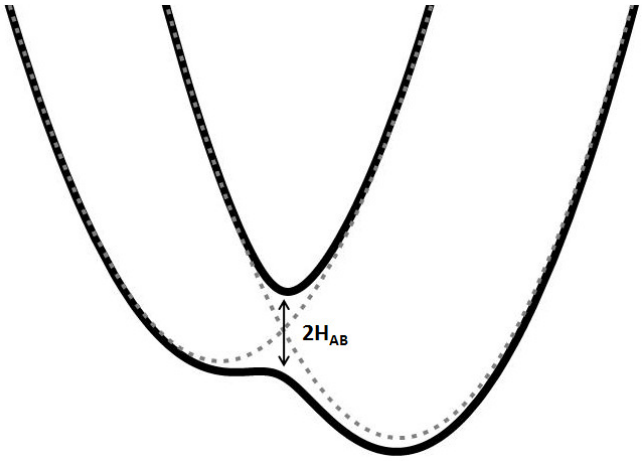

Figure 1.5. Adiabatic curves for an electron transfer reaction that result from a coupling of diabatic curves like the ones shown in Figure 1.3. Note that the extent of coupling is quantified by the electronic coupling term, H_{AB}.

From Eq. 1.8 and 1.9 as well as Figure 1.5, there are several important features we can note about these adiabatic curves. Firstly, at the point where the diabatic curves intersect (where H_{AA}=H_{BB})**,** the separation between the adiabatic curves is $2H_{AB}$. This is important because, as we

will see, H_{AB} is a measurable paremeter that lets us quantify the extent of electronic coupling. The other features of the adiabatic curves are direct results of the coupling provided by H_{AB}. With increasing coupling, the symmetric combination of diabatic curves (the bottom adiabatic curve) resembles the diabatic curves less and instead forms a new curve. As this happens, the thermal barrier to electron transfer decreases, the minima move closer together, and any change in free energy between the diabatic curves is less pronounced in the adiabatic curve.

1.5 Mixed Valence compounds and their Electronic Transitions

At this point it will be useful to move from general theories to more specific terms. The research described later in this report is on a series of mixed-valence compounds. Mixed valence (MV) compounds are compounds with redox centers connected by a bridging ligand which have an overall odd charge. They are often of the form $[M\text{-}L\text{-}M]^+$, where two metal centers (M) are connected by an organic bridge (L).

With the overall odd charge, the general questions involved in MV research become: (1) where does the charge reside, and (2) how easily does charge move from one redox center to the other? On one extreme, if the bridging ligand does not couple the redox centers well, the charge will reside on one redox center: $M^+\text{-}L\text{-}M$. At the other extreme, if the bridging ligand couples the redox centers extremely well, the charge will be distributed over both redox centers: $M^{+0.5}\text{-}L\text{-}M^{+0.5}$.

The Robin and Day system[4] classifies MV compounds based on the extent of charge delocalization. Class I compounds have essentially non-interacting redox sites; their potential energy curves look very similar to their parent diabatic curves. Class II compounds have coupled redox centers, but the charge is still localized. Their adiabatic curves are double-welled, with

$0 < H_{AB} < \lambda/2$. Class III compounds have fully delocalized charges. Their adiabatic curves have a single minimum and $H_{AB} > \lambda/2$.

Electronic absorption spectroscopy is an extremely useful tool to probe the extent of charge delocalization in MV compounds. Consider the Class I extreme, where the potential energy curves look like the diabatic curves shown in Figure 1.3. In the initial state (the *r* curve), the electron sits on one side of the molecule, and the bond lengths of the coordinated ligands and the solvent orientation reflect this. Upon absorbing light of sufficient energy, the electron can transition to the final state (the *p* curve) directly above the initial state minimum. Because electron transfers are much faster than nuclear movement, the bond lengths and solvent orientation will still be in their original positions, but the electron will have transferred from donor to acceptor. In this case, where the electron clearly goes from a donor site to acceptor site, the transition is called an intervalence charge transfer (IVCT).

As the redox centers become more coupled, the potential energy diagram looks more like that shown in Figure 1.5. In the extreme case (where the compound looks like $M^{+0.5}$-L-$M^{+0.5}$), the term IVCT no longer makes sense, and the transition is better termed "charge resonance band."

The optical absorption of MV compounds with this two-state treatment has been discussed in detail by Brunschwig and co-workers[5]. A summary of potential energy curve shapes and corresponding absorption spectra is shown in Figure 1.6[6]. Note that as a system moves from valence trapped (Class I and Class II) to delocalized, the absorption spectra changes from a broad Gaussian-shaped band to an asymmetric band (Class II-III border) to a sharp symmetric band (Class III). In the Class III extreme, the magnitude of coupling can be easily measured, as the absorption occurs at $E = 2H_{AB}$.

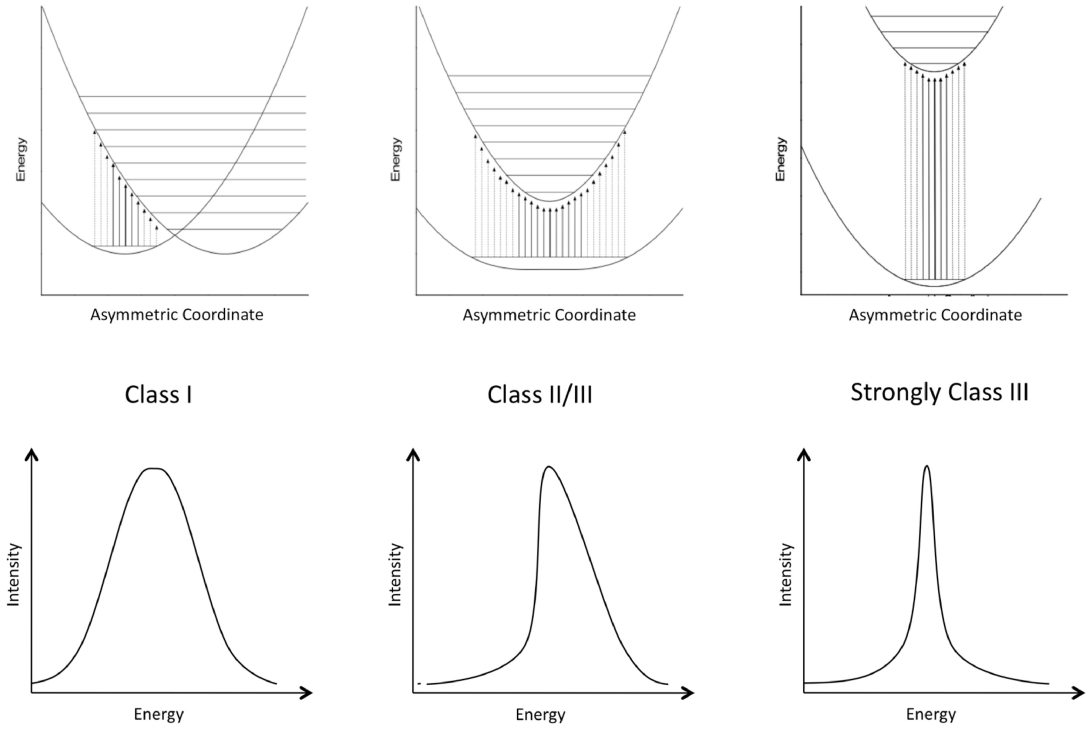

Figure 1.6[6] Schematic diagram showing how the shape of the IVCT band for symmetric systems under the two-state model changes as a function of coupling. (top) Potential energy surfaces with vibrational levels shown and (bottom) the associated band shapes.

2. Electronic communication facilitated by a metal-metal quadruple bond

Mixed valence compounds have received much attention for their utility in studying electron transfer. Focusing on the inorganic variety, we see that most mixed valence compounds have metal redox centers connected by an organic bridge, where compounds are oxidized. The most famous mixed valence ion, the Creutz-Taube ion[7], is an example of this architecture. This is also true in the Chisholm lab, where we often focus on compounds with two dimetal centers connected by a dicarboxylate bridge.

Inorganic mixed valence anions seem to be less common. Some of Hupp's MV compounds are anions, but the mechanism of electron transfer was determined to be the direct π-π coupling of bridging ligands.[8-10] Prior to this study, there seemed to be no direct anionic analogs to the typical cationic compounds, where two ligand based redox centers are bridged by a metal center that electronically couples them. While there was evidence of this type of mixed valency in a study of M_2(2,4,6-triisopropylbenzoate)$_2$(L)$_2$ where M=Mo or W, and L=azulene carboxylate[11-13] or L=thienylthiocarboxylate[14]. these compounds (as with many organic anion radicals) were kinetically labile, and were not chemically persistent.

In an effort to study ligand-based mixed valency, we have sterically and energetically protected ligand-based radical anions connected to MM centers. The resulting compounds are of the form $[L\text{-}[M_2]\text{-}L]^-$, the anion equivalent of the more common MV architecture in the Chisholm lab, $[[M_2]\text{-}B\text{-}[M_2]]^+$. The molecular orbital diagrams in Figure 2.1 compare the two architectures. In studying our MV anions, we will see many connections to their cation counterparts.

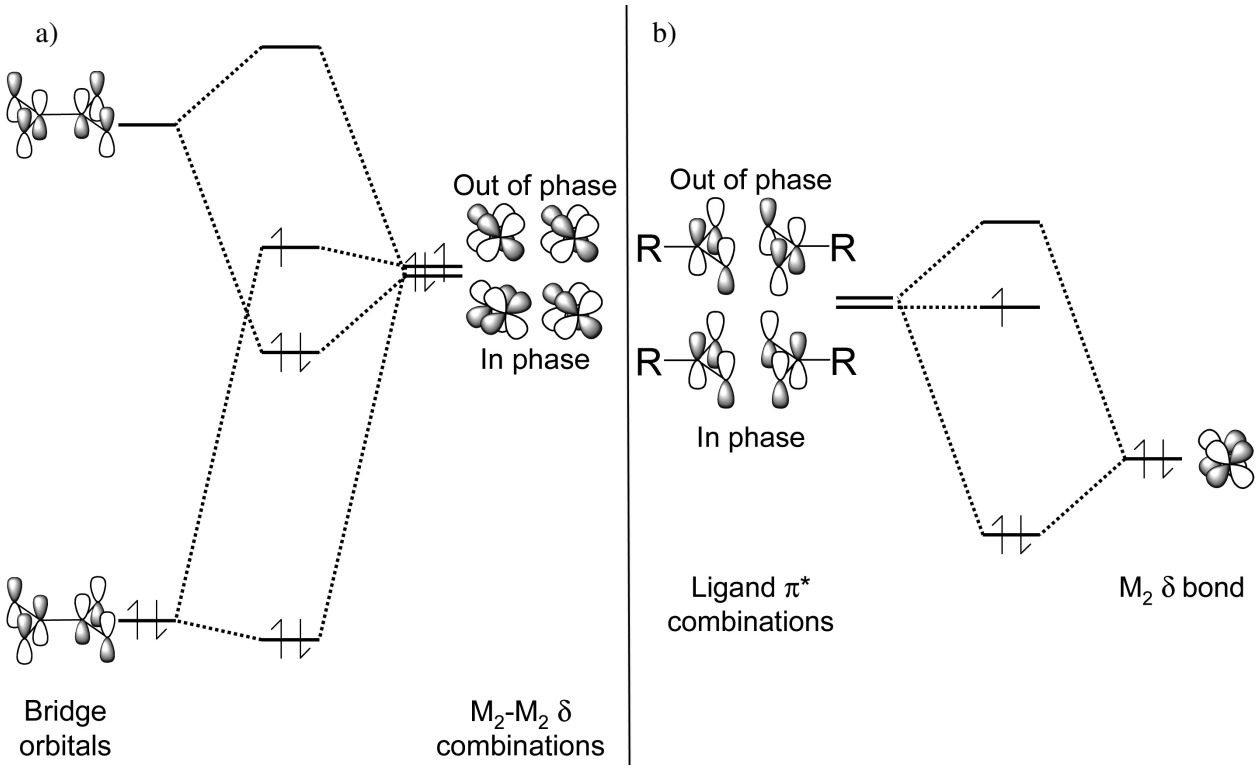

Figure 2.1. Schematic molecular orbital diagrams for (a) $[[M_2]\text{-B-}[M_2]]^+$ complexes, and (b) $[L\text{-}[M_2]\text{-}L]^-$. Note that in each case it is the π* system of the bridge/ligand that couples with the M_2 δ orbitals.

Much of the following has been taken directly from the corresponding publication by Bunting, Chisholm, and coworkers.[6]

2.1 Results and Discussion

Synthesis

The reaction between $W_2(TiPB)_4$ and 4-isonicotinic acid (2 equivalents) in toluene gave $W_2(TiPB)_2(nic)_2$, **2**, where TiPB is 2,4,6-triisopropylbenzoate and nic is 4-isonicotinate with the liberation of TiPBH (2 equivalents). This green crystalline compound is analogous to the previously reported $Mo_2(TiPB)_2(nic)_2$, **1**, which has a trans-disposition of ligands and exists as a coordination polymer in the solid-state due to weak N-to-M axial ligation.[15]

The reactions between either **1** or **2** and $B(C_6F_5)_3$ (2 equivalents) in THF proceed smoothly at room temperature to give **1B** (M=Mo) and **2B** (M=W). These reactions proceed with a distinct color change: **1** (red) → **1B** (purple) and **2** (green) → **2B** (pale blue).

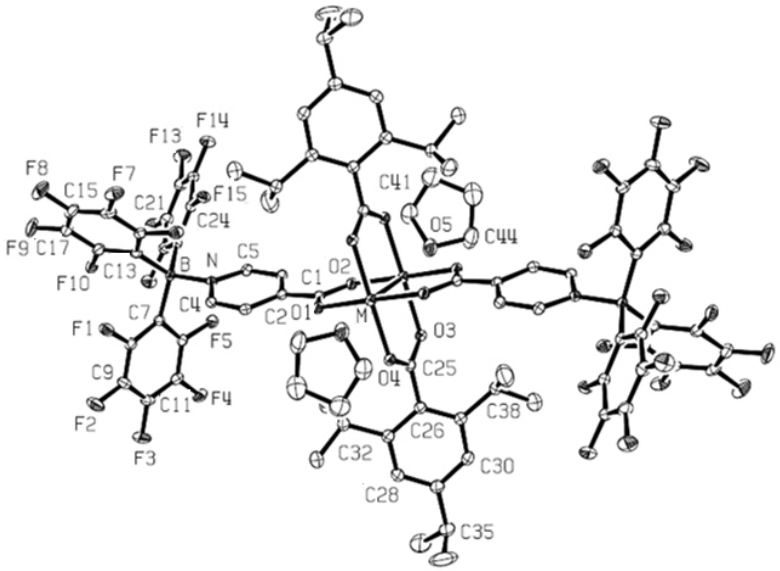

Figure 2.2. ORTEP drawing of **2B** (M=W) The ORTEP plot is drawn with 30% probability ellipsoids for the non-hydrogen atoms. The hydrogen atoms are omitted for clarity. The molecule contains a crystallographic inversion center, which is located in the middle of the W-W bond. The solvent molecule of *n*-hexane is also omitted from this plot.

Crystals of **1B** adequate for single-crystal X-ray diffraction were grown from a THF/hexane solution. Similar crystals of **2B** were grown in cold toluene. Both molecules crystallized in the *P-1* space group, and they are isostructural. They have a crystallographically imposed center of inversion located at the midpoint of the M-M bond. The molecular structure of the tungsten compound, **2B**, is shown in Figure 2.2. The central $M_2(O_2C)_4$ core is typical of MM quadruply bonded compounds supported by carboxylates.[16] The two isonicotinate ligands are mutually trans and the O_2C and C_5N planes are aligned so as to allow extended ligand π-M_2 δ-ligand π interactions. The dihedral angles between the O_2C and C_5N least-squares planes are

12.8(2)° in **1B** and 13.5(3)° in **2B**. A similar pattern of $M_2(TiPB)_2(O_2C\text{-thienyl})_2$[14] compounds and in the compound $W_2(TiPB)_2$(6-carboethoxy-2-azulenecarboxylate)$_2$.[13] The slight curvature of the extended π system in these compounds is reminiscent of that seen in dinuclear polyyne bridged complexes, $[M]\text{-}(C_2)_n\text{-}[M]$.[19] Finally, the central $[M_2]$ unit has weak axial coordination of the THF molecules with long M···O distances (>2.5 Å) in contrast to the M—O carboxylate distances, which fall in the range of 2.05—2.10 Å. Selected bond distances for the two compounds are given in Table 2.1.

	Distance, Å	
Bond	**1B**	**2B**
M-M	2.1153(4)	2.5158(3)
O(1)-M	2.1098(14)	2.065(2)
O(2)-M	2.0935(14)	2.048(2)
O(3)-M	2.0984(14)	2.072(2)
O(4)-M	2.0946(14)	2.074(2)
O5-M	2.564(3)	2.525(3)
N-B	1.624(3)	1.615(4)

Table 2.1. Selected Bond Distances for **1B** and **2B**

Electronic Structure Calculations

In order to aid in the interpretation of the spectroscopic and electrochemical data pertaining to the complexes **1**, **1B**, **2**, and **2B**, we undertook electronic structure calculations on model compounds (**1'**, **1B'**, **2'**, and **2B'**), where formate is substituted for the TiPB ligands. This substitution saves on computational time and is not an unreasonable approximation since the TiPB rings are twisted out of conjugation with their carboxylate linkers. The gas-phase minimum energy structures were determined in C_1 symmetry and possessed the planar alignment of the two trans $O_2C\text{-}C_5H_4N$ units.

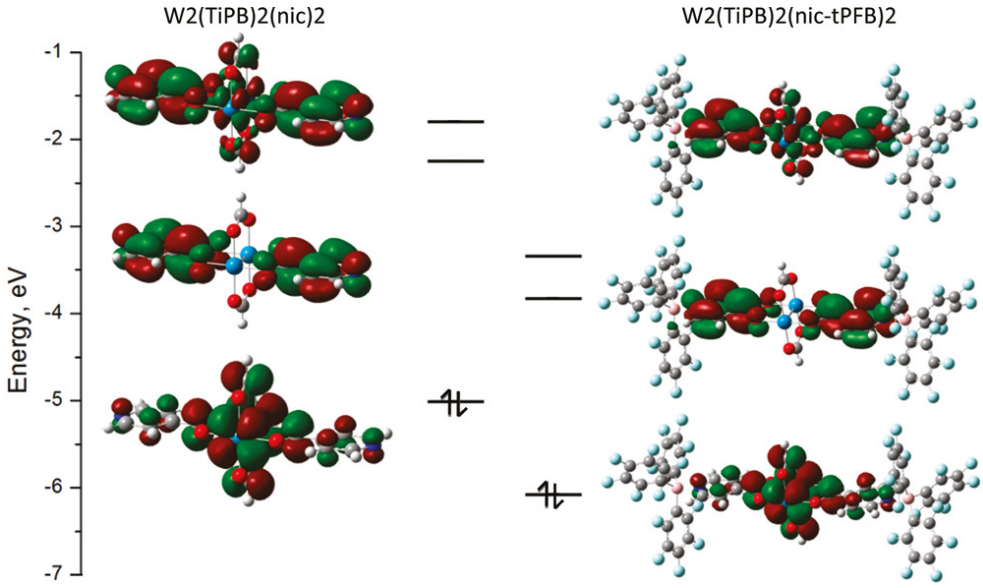

Figure 2.3. Energy level diagram for **2'** and **2B'** showing the HOMO, LUMO and LUMO+1

For **1'**, **1B'**, **2'**, and **2B'**, the HOMO was the $M_2\delta$ orbital with some mixing with the isonicotinate ligands. For **1B'**, **2'**, and **2B'**, the LUMO and LUMO+1 were, respectively, the in-phase and out-of-phase combinations of the ligand π* orbitals, as predicted by the schematic MO interaction diagram shown in Figure 2.1. However, for **1'**, these combinations were the LUMO+1 and LUMO+2, the LUMO being the MM δ*. The comparison between the model compounds **1'** and **1B'**, as well as **2'** and **2B'**, reveals some striking trends. (i) Complexation to $B(C_6F_5)_3$ notably stabilizes the energy of the $M_2\delta$ orbital (HOMO). (ii) The LUMO is also stabilized, but to a greater extent, thus reducing the HOMO—LUMO gap upon complexation with $B(C_6F_5)_3$. (iii) Complexation to $B(C_6F_5)_3$ has little effect on the energy gap between the in-phase and out-of-phase combinations of the lowest energy ligand π* orbitals. These changes are illustrated by the comparison of the calculated frontier molecular orbital energies for compounds **2'** and **2B'**, as shown in Figure 2.3. The calculated energies of these frontier orbitals are given in Table 2.2.

Compound	HOMO δ	δ*	L π_1*	L π_2*	ΔE
1	-5.48	-2.24	-2.19	-1.86	0.33
1B	-6.46	-3.19	-3.75	-3.43	0.32
2	-5.01	-1.50	-2.25	-1.79	0.46
2B	-6.07	-2.52	-3.83	-3.35	0.48

[a] L π* = in-phase combination (LUMO or LUMO+1); L π_2* = out-of-phase combination (LUMO+1 or +2); ΔE = L π_2* - L π_1*.

Table 2.2. Calculated Frontier MO Energies (eV)[a]

We also note that as a result of the 3-fold symmetry of $B(C_6F_5)_3$, it is not well matched to electronically couple the aryl rings to the nic donor (as seen in Figure 2.3). For this reason, complexation of $B(C_6F_5)_3$ to **1** and **2** affects the energies of the nic π and $M_2\delta$ orbitals without substantially affecting their nature and thus, affects the energy, but not the nature, of the electronic transitions in these complexes.

Electronic Absorption Spectra

The room-temperature optical spectra of the four compounds, **1**, **1B**, **2**, and **2B** are shown in Figure 2.4. The intense absorptions in the visible region arise from the $M_2\delta$ to isonicotinate π*, ^{1}MLCT transition. The trends in the energies associated with this transition correlate well with the expectations based on the calculated HOMO—LUMO gaps as can be seen from an inspection of Figure 2.1. The intensity of the MLCT transitions increases with decreasing energy, and the ε values range from 9200 M^{-1} cm^{-1} for **1** to 38000 M^{-1} cm^{-1} for **2B**. Such a trend is expected, because coupling between the ligands and the M_2 center (and, hence ε) will increase as the energy gap between them decreases.

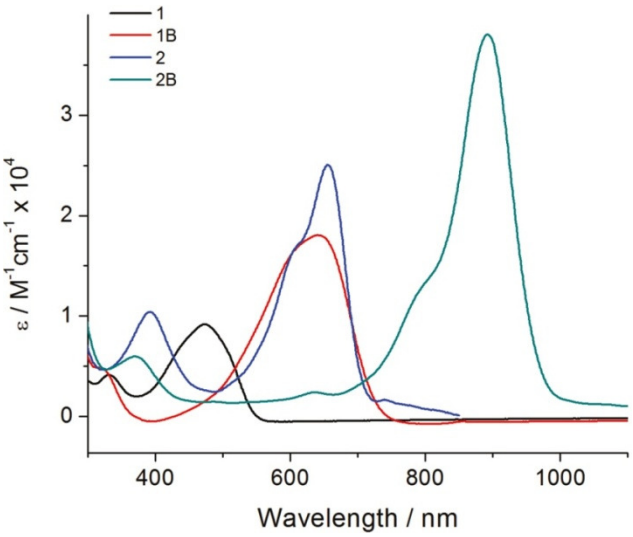

Figure 2.4. UV-vis spectra for **1**, **1B**, **2**, and **2B** in THF at room temperature

We also comment that, in solution, there is a Boltzmann distribution of rotamers deviating from the ground-state planar D_{2h} conformation, and each of these gives rise to a slightly different MLCT transition energy. Either an increase in π* back-bonding or a reduction of the temperature will favor the D_{2h} conformation, shifting the weighted distribution toward planarity. This reasoning explains the fact that the red shift of these ^{1}MLCT bands (**1→2B**) is accompanied by a decrease in bandwidth, consisten with enhanced $M_2\delta$ to nic π* back-bonding (as the $M_2\delta$—nic π* energy gap decreases). Furthermore, lowering the temperature is found to lead to a sharpening of the vibronic features, as a more planar structure in the compounds is reinforced. A comparison of the room-temperature spectra of **1B** and **2B** to those at 100 K (recorded in 2-MeTHF) is given in Figure 2.5.

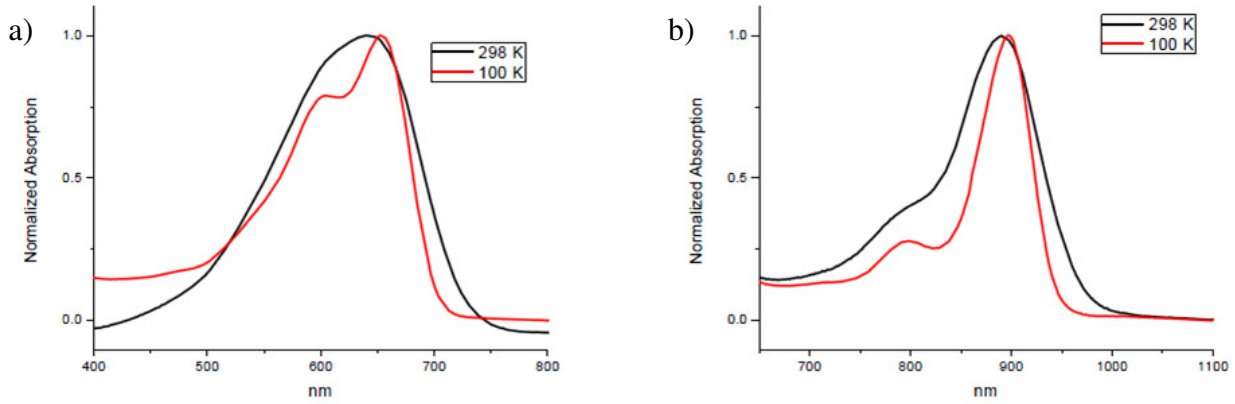

Figure 2.5. MLCT band for (a) **1B** and (b) **2B** at both room temperature (black) and 100 K (red line) in 2-MeTHF

We have also examined the solvent dependence of the ^{1}MLCT for compounds **1B** and **2B** in toluene, dichloromethane, and THF. These spectra are shown in Figure 2.6. For both compounds, the spectra in THF are red-shifted relative to the other solvents, which is not surprising because THF can coordinate to the M_2 center (as seen in Figure 2.2) and destabilize the M_2 δ orbital, thus reducing the HOMO—LUMO gap. The spectra for the molybdenum complex, **1B**, in CH_2Cl_2 and toluene have λ_{max} at 626 and 599 nm, respectively, while for the tungsten complex, **2B**, λ_{max} is at 850 for both CH_2Cl_2 and toluene. We propose this reflects the greater delocalization of the ligand-based negative charge in the case of the tungsten complex, **2B**. In other words, the ^{1}MLCT for **2B** has a neglibible change in dipole moment, while that for **1B** has at least some change. Note that the dielectric constants for CH_2Cl_2 and toluene are 8.93 and 2.38, respectively. This significant difference makes them good solvents for evaluating the relative change in dipole moment for a MLCT transition.

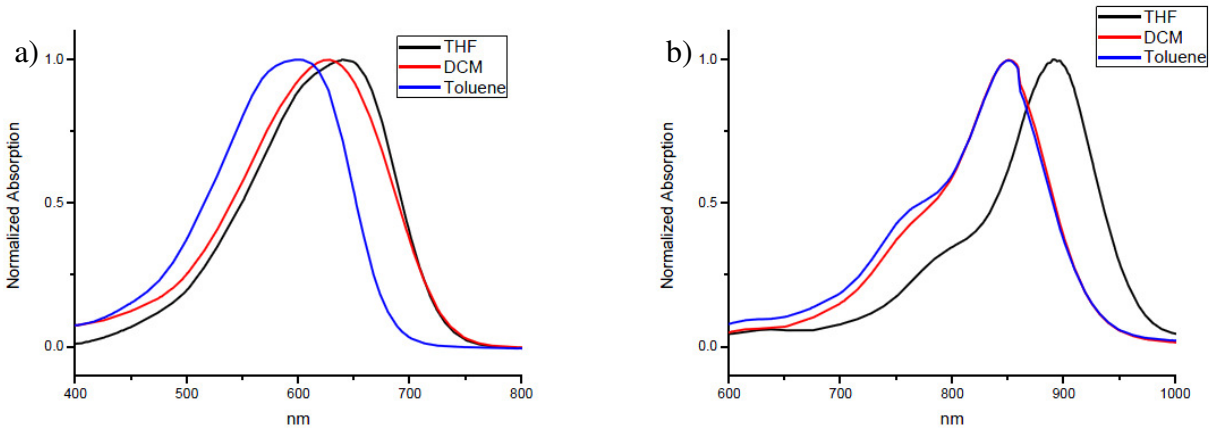

Figure 2.6. MLCT band for (a) **1B** and (b) **2B** taken in THF (black), dichloromethane (red), and toluene (blue).

Electrochemical Data

The four compounds under study have been examined by cyclic voltammetry and differential pulse voltammetry in THF solutions. The data are summarized in Figure 2.7 and Table 2.3. All four compounds show three redox events. The most positive of these is associated with the removal of a single electron from the M_2^{4+} core. The remaining two events, which occur at much more negative potentials, are both one-electron reductions of the ligands. As expected, it was found that it was easier to oxidize the W_2^{4+} center than the Mo_2^{4+} and that complexation with $B(C_6F_5)_3$ shifts these oxidation potentials to more positive values. Similarly, the ligand based reduction waves occur at a less negative potential in the $B(C_6F_5)_3$ adducts, relative to **1** and **2**. These results are in line with expectations based upon the calculations on the model compounds (2.2) as well as with chemical intuition.

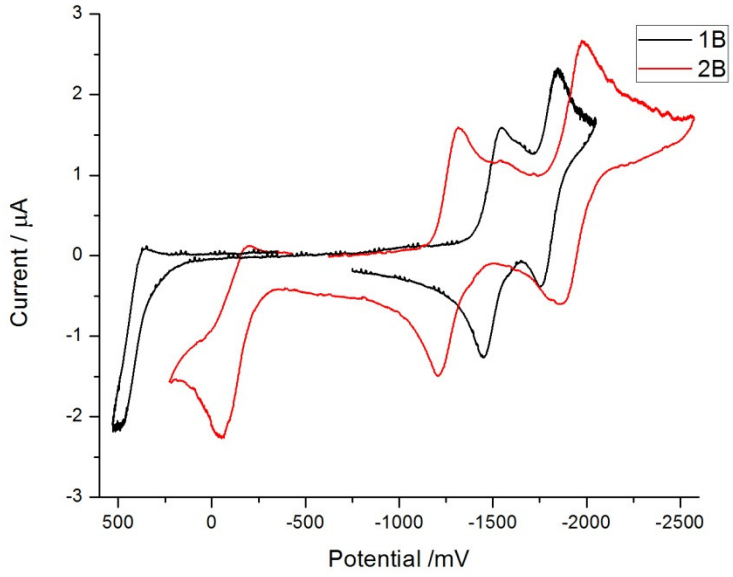

Figure 2.7. Cyclic voltammograms of compounds **1B** and **2B** in THF showing the metal based oxidation and the ligand based reductions. The mV scale is referenced to the Cp2Fe0/+ couple.

Complex	E_1	E_2	E_3	$\Delta E_{2,3}$
1	-0.02	-2.48	-2.60	0.12
1B	0.42	-1.50	-1.80	0.30
2	-0.24	-1.88	-2.32	0.44
2B	-0.13	-1.27	-1.92	0.65

Table 2.3. Redox potentials (V) for the three redox events observed for **1**, **1B**, **2**, and **2B** in THF referenced to the Fc/Fc^+ couple

Of particular note is the magnitude of the splitting between the reduction waves. The splitting reflects a combination of the magnitude of the electronic coupling and electrostatic effects, which vary with solvent and counterions. However, for pairs of related ions that differ only by metal ions Mo vs. W, which have effectively identical size and solvent effects, the magnitude of the separation of the two waves is informative with respect to the relative electronic coupling of the two isonicotinic ligands via the $M_2\delta$ orbital. The splitting is 0.12, 0.30, 0.44, and 0.65 mV for **1**, **1B**, **2**, and **2B**, respectively. notably, the magnitude of this coupling is always bigger for the tungsten complexes due to the greater $W_2\delta$—ligand π^*

interactions. Upon adduct formation with $B(C_6F_5)_3$ there is a further increase in separation, which is due to the stabilization of the negative charge on the ligands by the $B(C_6F_5)_3$. This also has the effect of increasing the coupling (relative to **1** and **2**) of the ligand-based states with the lower energy M_2-based state.

Inspection of the reduction waves for the tungsten complex **2B** reveals the presence of an additional species with a reduction potential slightly more negative than the first event. The sample under investigation was taken from the crystals that were subject to elemental anaylsis, so we are not inclined to view that the sample was impure. Rather, we propose that under the dilute condition of **2B** in the donor solvent THF some equilibrium exists where one $B(C_6F_5)_3$ unit dissociates from a nic ligand. Some support for this is seen in the electrochemical behavior of **2B** in dichloromethane, where this extra reduction is not observed. In CH_2Cl_2, the second reduction is found to be irreversible. A similar feature is seen in the electrochemistry of **1B** in THF. However, **1B** is not sufficiently soluble in CH_2Cl_2, and we assume that this has similar origins.

*Mixed Valence ions: **1B**$^-$ and **2B**$^-$*

Reduction of **1B** and **2B** with Cp_2*Co in THF gave reduced ions **1B**$^-$ and **2B**$^-$ whose spectral features are shown in Figure 2.8. Upon reduction of **1B** to **1B**$^-$, the color of the solution changed from blue to green. there was a very slight change of color upon reduction of **2B** to **2B**$^-$, mainly changing the shade of blue-green. Of prime significance is the appearance of new sharp electronic bands in the NIR region, namely at 3800 cm^{-1} for **1B**$^-$ and 4500 cm^{-1} for **2B**$^-$. These bands are sharp, with the width at half height for **2B**$^-$ being only 300 cm^{-1}. In addition, we note that the band for **1B**$^-$ is noticeably more asymmetric than that for **2B**$^-$. We assign these bands to

the charge resonance transitions of fully delocalized mixed valence ligands. In a simple MO description (Figure 2.1), they correspond to the promotion of the single electron from the LUMO to the LUMO+1. This is consistent with the similarity of the EPR spectra of **1B**$^-$ and **2B**$^-$ (discussed below).

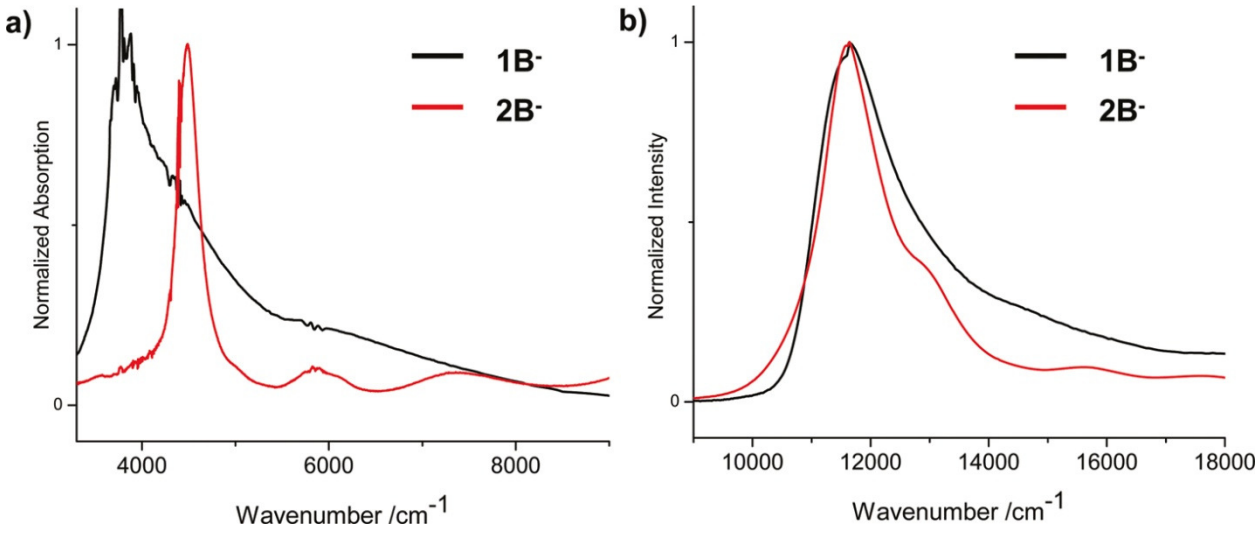

Figure 2.8. Comparison of the (a) IVCT and (b) MLCT bands of **1B** and **2B** in THF at room temperature. All of the bands are presented normalized for ease of comparison.

In addition to the electronic transition in the NIR, each compound also shows a strong absorption in the visible region corresponding to the ^{2}MLCT. In orbital terms, this is promotion of a single electron from the $M_2\delta$ orbital to the SOMO. The ^{2}MLCT band for **1B**$^-$ is lower in energy than that for **1B** and that for **2B**$^-$ is higher in energy than that for **2B**. Also, the ^{2}MLCT bands are narrower than their singlet counterparts. Finally, based on the shape of these electronic NIR transitions, we assign **1B**$^-$ as near the Robin-Day Class II/III border and **2B**$^-$ well within class III.

*EPR Spectrum of **1B**$^-$ and **2B**$^-$*

Reduction of **2B** with Cp_2^*Co in THF leads to an EPR-active species, **2B**$^-$, that has a single resonance at g≈2.04. This shows no hyperfine coupling to ^{183}W and, in contrast to tungsten-based $W_2\delta^1$ electrons with g≈1.8, is close to the free electron value. This is consisten with a ligand-centered radical anion. Reduction of **1B** with Cp_2^*Co similarly leads to an EPR-active species with a single resonance at g≈2.01, consistent with a ligand-centered radical anion. This signal showed no hyperfine coupling to ^{95}Mo or ^{97}Mo.

Comparisons with Oxalate Bridged M_2 Containing Complexes

We are struck by the remarkable relationship between the spectra and the electrochemical data for the MV ions that result for the oxalate-bridged species of the form $[(Bu^tCO_2)_3]_2$-μ_2-$(O_2C\text{-}CO_2)^+$ and the anions **1B**$^-$ and **2B**$^-$. As is evident from Figure 2.1, the radical cations are metal-centered and the anions are ligand-centered. For the former, the splitting of the $M_2\delta$ orbitals in the neutral complexes is a measure of the electronic coupling of the two M_2 centers. For molybdenum, this is ≈0.3 eV, while for tungsten, this is ≈0.5 eV. For **1B**' and **2B'**, the energy of the separation of the in-phase and out-of-phase ligand π* orbitals (0.32 and 0.48 eV, respectively) is also a measure of the coupling of the ligand π systems in the neutral complexes. Upon oxidation of the former and reduction of the latter, the coupling will increase in the resultant MV ions, as we have previously discussed[20], because the MO picture does not accurately reflect the nature of coupling between the electronic *states*. Nevertheless, the fact that the calculated energy separation between the in-phase and out-of-phase ligand π* orbitals in the anions (**1B**$^-$ and **2B**$^-$) is virtually identical to the separation of the two $M_2\delta$ combinations in the oxalate-bridged cations seems more than fortuitous.

This similarity of calculated energy splitting is remarkably born out in the observed electrochemical and spectroscopic features of the related cations and anions, as can be seen from an inspection of Table 2.4. As $\Delta E_{1/2}$ increases so does the ν_{max} of the charge resonance band, which is consistent with Class III behavior. The shape of the charge resonance bands also tracks with H_{AB}, and as H_{AB} increases, the bands get sharper and more symmetric. For a comparison, we show the IVCT bands of the oxalate bridged cations in Figure 2.9. Perhaps the only major difference in comparing the radical cations and the anions is in the bandwidths of these charge resonance transitions. The MV anions are notably sharper, and the $\Delta\nu_{1/2}$ of 300 cm^{-1} for **2B**$^-$ is truly remarkable.

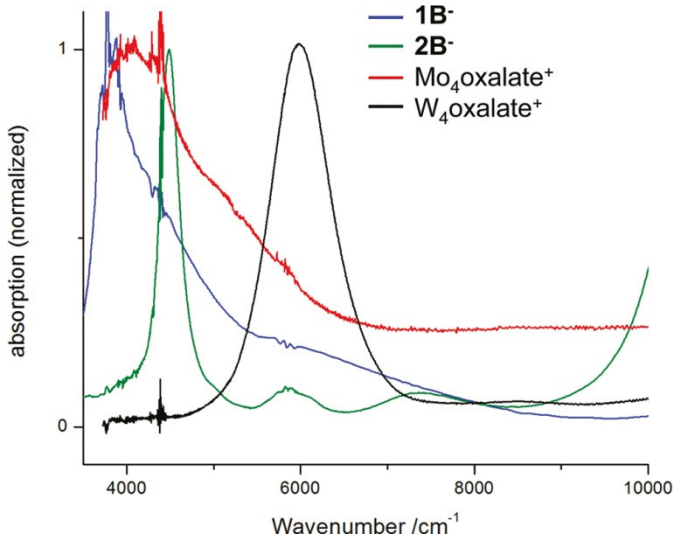

Figure 2.9. Comparison of the IVCT bands for the mixed valence anions **1B**$^-$ (blue) and **2B**$^-$ (green) with the IVCT bands for the mixed valence cations Mo_4oxalate$^+$ (red) and W_4oxalate$^+$ (black). All spectra were taken in THF.

Complex	$\Delta_{1/2, mV}$	K_c [a]	N_{max}, [b] cm^{-1}	$\Delta\nu_{1/2}$, [b] cm^{-1}	H_{AB}, [c] cm^{-1}
1B$^-$	300	1.22×10^5	3800	1000	1900
2B$^-$	650	1.04×10^{11}	4500	300	2250
Mo$_4$oxalate$^+$	280	5.57×10^4	4000	2800	2000
W$_4$oxalate$^+$	717	1.42×10^{12}	5960	940	2980

[a] $K_c = \exp(\Delta E_{1/2}/25.69)$ at 298 K. [b] For the IVCT bands. [c] Assuming the Class III limit, where $H_{AB} = \nu_{max}(cm^{-1})/2$

Table 2.4. Comparison of Select Parameters for ligand- and metal-based mixed valence complexes

The similar relationships noted above between the cations $[M_2\text{-B-}M_2]^+$ and the anions $[L\text{-}M_2\text{-}L]^-$ may, in part be related to the distance between the two redox-active centers. For the oxalate-bridged system, the M_2 centers are 6 Å apart, while in **1B** and **2B**, the *ipso*-carbons of the nic ring are similarly separated by the $M_2\text{-}(O_2C)_2$ unit at a distance of 8 Å.

Conclusions

By energetically and sterically stabilizing the organic radical anion formed upon reduction of **1B** and **2B**, we have created a system which allows us to study the electronic communication facilitated by the MM quadruple bond. Using the IVCT band shapes from the NIR absorption, we have assigned **1B$^-$** and **2B$^-$** as Class II/III and Class III mixed-valence ions, respectively. In comparing the anions **1B$^-$** and **2B$^-$** with the $M_2\text{-}\mu_2$-oxalate cations, we see a remarkable similarity in IVCT behavior. We propose that this similarity arises for two principle reasons. (1) The distances between the two redox centers, the two M_2 centers in the oxalate-bridged cations, and the isonicotinic ligands are similar. (2) In both cases, the coupling arises via M_2 $\delta\text{-}CO_2$ π^* orbital interactions, and the energy separation between the M_2 δ HOMO and the bridge/ligand LUMO is of comparable energy.

2.2 Experimental

All reactions were carried out under dry and inert atmosphere (N_2 or argon) using standard Schlenk and glovebox techniques. All solvents were dried and degassed by standard methods and distilled prior to use. Ditungsten and dimolybdenum tetratriisopropylbenzoate (MO_2TiPB_4 and W_2TiPB_4, respectively) were prepared by the literature procedure.[13,14] Isonicotinic acid (Hnic) and $B(C_6F_5)_3$ were purchased from commercial sources and used as received. Decamethylcobaltocene was purchased from commercial sources and sublimed prior to use. Preparation of **1** has previously been reported.[15]

Instrumentation

UV-vis and NIR spectra were collected on a Perkin-Elmer Lambda 900 UV-vis-NIR spectrometer. Low-temperature UV-vis spectra were acquired on the same UV-vis spectrophotometer using a Specac variable-temperature cryostate that employs a permanently sealed liquid IR cell with CaF_2 windows. EPR spectra were acquired at room temperature on a Bruker ESP300 in 2-MeTHF or THF.

*Preparation of $W_2(TiPB)_2(nic)_2 \cdot THF$ (**2**)*

A Schlenk flask was charged with 1 equivalent of W_2(triisopropylbenzoate)$_4$ and 2 equivalents of isonicotinic acid. On a Schlenk line, enough acetonitrile was added to the flask to fully dissolve the $W_2(TiPB)_4$, though the isonicotinic acid was not completely soluble. The resulting solution was stirred for 3 days, at which time no solid isonicotinic acid remained in the flask. During the course of the reaction, the solution had changed from bright red to green, and a

green precipitate was formed. The solid was collected by centrifugation and washed three times with hexanes and then dried under vacuum. Yield 40%.

Anal. Calc for $W_2C_{44}H_{54}N_2O_8$: C, 48.91; H, 5.30; N, 2.38. Found: C, 48.63; H, 5.07; N, 2.20. ^{1}H NMR (250 MHz, THF-d_8): δ 1.0 (d, 12H), 1.3 (d, 6H), 2.9 (m, 3H), 7.1 (s, 2H), 8.5 (d, 2H), 9.1 (d, 2H).

*Preparation of $Mo_2(TiPB)_2(nic\text{-}B(C_6F_5)_3)_2$, (**1B**)*

A Schlenk flask was charged with 1 equivalent of **1** and 2 equivalents of $B(C_6F_5)_3$ in a glovebox. On a Schlenk line, enough THF was added to dissolve **1**. The reaction was left to stir for two days during which time the solution changed color from red to blue. After this, the THF was removed under vacuum to a minimal volume. To this, hexanes were added in order to crash out the desired product, which was collected via centrifugation and washed three times with hexanes. The product was then dried, and the solid was collected. Yield 65%.

Anal. Calcd for $Mo_2C_{80}H_{54}B_2F_{30}N_2O_8$: C, 49.15; H, 2.79; N, 1.43. Found: C, 48.93; H, 2.85; N, 1.39. ^{1}H NMR (250 MHz, THF-d_8): δ 1.0 (d, 12H), 1.3 (d, 6H), 2.9 (m, 3H), 7.1 (s, 2H), 8.5 (d, 2H), 9.1 (d, 2H).

*Preparation of $W_2(TiPB)_2(nic\text{-}B(C_6F_5)_3)_2\cdot THF$ (**2B**)*

Compound **2B** was made in a similar manner as **1B**. Alternatively, **2B** was made by charging one flask with 1 equivalent W_2(triisopropylbenzoate)$_4$ and a second flask with 2 equivalents of isonicotinic acid and 2 equivalents of $B(C_6F_5)_3$ in a glovebox. To the second, toluene was added on a Schlenk line, and the solution stirred until the isonicotinic acid was completely dissolved. This solution was then transferred to the first flask. Upon the addition of

the solution, the color of the reaction changed from bright red to emerald green and, finally, to blue. The reaction was stirred for 3 days and then placed in a refrigerator at 10 °C for 2 weeks after which time crystals appropriate for X-ray diffraction were found to have grown in the flask. A few crystals were removed for X-ray diffraction; the rest were washed three times with hexanes and dried in vacuum. Yield 34%.

Anal. Calcd for $W_2C_{84}H_{62}B_2F_{30}N_2O_9$: C, 46.46; H, 3.10; B, 0.95; N, 1.23. Found: C, 46.10; H, 3.37; B, 0.52; N, 1.36. ^{1}H NMR (250 MHz, THF-d_8): δ 1.0 (d, 12H), 1.2 (d, 6H), 2.8 (m, 3H), 7.0 (s, 2H), 8.2 (d, 2H), 9.0 (d, 2H).

*Preparation of the Anions **1B**$^-$ and **2B**$^-$*

The reactions between solutions of **1B** or **2B** and Cp_2*Co in either THF or 2-MeTHF were carried out in a 1:1 ratio yielding an immediate color change. These freshly prepared solutions were then examined by EPR and UV-vis-NIR spectroscopy. The following represents an initial attempt to isolate a salt in a pure microcrystalline form.

$Mo_2(TiPB)_2(nic\text{-}B(C_6F_5)_3)_2$, **1B** (31.7 mg, 0.0162 mmol), and $CoCp_2$* (5.5 mg, 0.017 mmol) were put in separate Schlenk flasks. Compound **1B** was dissolved in minimal THF and cooled in an ice bath, while the $CoCp_2$* was dissolved in excess hexanes. The $CoCp_2$* solution was transferred to the solution of **1B**, causing an immediate color change from blue to green and a green precipitate to fall out of solution. The mixture was stirred for 2 min, and then the green precipitate was collected via filtration, washed three times with ehxanes, and dried under vacuum. Yield 29.8 mg, 0.0130 mmol, 80%

Anal. Calcd for $Mo_2C_{100}H_{84}B_2F_{30}N_2O_8Co$: C, 52.58; H, 3.71; N, 1.23. Found C, 49.00; H, 4.08; N, 0.97.

DFT Calculations

Molecular and electronic structure determination were performed under C_1 symmetry using the Gaussian 98 program[23] emplying the B3LYP functional[24-26] in conjugation with the 6-31G* basis set[27] for H, C, O, N, and B and the SDD energy-consistent pseudopotential basis set[28] for Mo and W. All geometries were fully optimized at the above levels using the default optimization criteria of the program. Orbital analyses were completed with GaussView.[29]

Acknowledgements

Many thanks to Professors Malcolm Chisholm and Christopher Hadad, who are responsible for my early entry to undergraduate research and who have continued to help me with both my academic and professional goals. In the same vein, the Beckman Scholars Program funded me in 2009-2010 and has opened many other doors for me. Thanks also to Professor Ben Lear for teaching me the necessary lab techniques as well as for being my main source of mixed valence material. Dr. Vesal Naseri has been my main editor for this and several other documents and has been an excellent source of information on research outside of the mixed valence field. Finally thanks to my family for their constant support as well as for being the majority of the readership of this document.

References

(1) Marcus, R. A. *J. Chem. Phys.* **1956**, *24*, 966-978
(2) Miller, J. R.; Calcaterra, L. T.; Closs, G. L. *J. Am. Chem. Soc*. **1984**, *106*, 3047
(3) Sutin, N. *Prog. Inorg. Chem.* **1983**, *30*, 441-498
(4) Robin, M. B.; Day, P.; *Adv. Inorg. Chem. Radiochem*. **1967**, *10*, 247-403
(5) Brunschwig, B. S.; Creutz, C.; Sutin, N. *Chem. Soc. Rev.* **2002**, *31*, 168-184
(6) Bunting, P.; Chisholm, M. H.; Gallucci, J. C.; Lear, B. J. *J. Am. Chem. Soc.* **2011**, *133*, 5873-5881
(7) Creutz, C.; Taube, H. *J. Am. Chem. Soc.* **1969**, *91*, 3988–3989.
(8) Dinolfo, P. H.; Coropceanu, V.; Bredas, J.; Hupp, J. T. *J. Am. Chem. Soc.* **2006**, *128*, 12592–12593
(9) Dinolfo, P. H.; Hupp, J. T. *J. Am. Chem. Soc*. **2004**, *126*, 16814–16819
(10) Dinolfo, P. H.; Williams, M. E.; Stern, C. L.; Hupp, J. T. *J. Am. Chem. Soc*. **2004**, *126*, 12989–13001
(11) Barybin, M. V.; Chisholm, M. H.; Dalal, N. S.; Holovics, T. H.; Patmore, N. J.; Robinson, R. E.; Zipse, D. J. *J. Am. Chem. Soc*. **2005**, *127*, 15182–15190.
(12) Barybin, M. V.; Chisholm, M. H.; Patmore, N. J.; Robinson, R. E.; Singh, N. *Chem. Commun.* **2007**, 3652–3654.
(13) Alberding, B. G.; Barybin, M. V.; Chisholm, M. H.; Gustafson, T. L.; Reed, C. R.; Robinson, R. E.; Patmore, N. J.; Singh, N.; Turro, C. *Dalton Trans*. **2010**, *39*, 1979–1984.
(14) Alberding, B. G.; Chisholm, M. H.; Chou, Y.; Ghosh, Y.; Gustafson, T. L.; Liu, Y.; Turro, C. *Inorg. Chem.* **2009**, *48*, 11187–11195.
(15) Chisholm, M. H.; Dann, A. S.; Dielmann, F.; Gallucci, J. C.; Patmore, N. J.; Ramnauth, R.; Scheer, M. *Inorg. Chem.* **2008**, *47*, 9248-9255
(16) Cotton, F. A.; Murillo, C. A.; Walton, R. A. *Multiple Bonds between Metal Atoms*, 3rd ed.; Springer Science and Business Media, Inc.: New York, 2005; p 818
(17) Alberding, B. G.; Chisholm, M. H.; Chou, Y.; Ghosh, Y.; Gustafson, T. L.; Liu, Y.; Turro, C. *Inorg. Chem.* **2009**, *48*, 11187-11195
(18) Alberding, B. G.; Barybin, M. V.; Chisholm, M. H.; Gustafson, T. L.; Reed, C. R.; Robinson, R. E.; Patmore, N. J.; Singh, N.; Turro, C. *Dalton Trans.* **2009**, *39*, 1979-1984
(19) Szafert, S.; Gladysz, *J. A. Chem. Rev.* **2006**, *106*, 1–33.
(20) Lear, B. J.; Chisholm, *M. H. Inorg. Chem*. **2009**, *48*, 10954–10971.
(21) Barybin, M. V.; Chisholm, M. H.; Patmore, N. J.; Robinson, R. E.; Singh, N. *Chem. Commun*. **2007**, 3652–3654.
(22) Cotton, F. A.; Daniels, L. M.; Hillard, E. A.; Murillo, C. A. *Inorg.Chem*. **2002**, *41*, 1639–1644.
(23) Frisch, M. J.; et al. *Gaussian 98*, revision A6; Gaussian Inc.: Pittsburgh, PA, 1998.
(24) Lee, C.; Yang, W.; Parr, R. G. *Phys. Rev. B*: *Condens. Matter* **1988**, *37*, 785–789.
(25) Becke, A. D. *J. Chem. Phys*. **1993**, *98*, 5648–5652.
(26) Becke, A. D. *Phys. Rev A*: *Gen. Phys*. **1988**, *38*, 3098–3100.
(27) Hehre, W. J.; Radom, L.; Schleyer, P. V.; Pople, J. A. *Ab initio Molecular Orbital Theory*; Wiley: New York, 1986.
(28) Andrae, D.; iuBermann, U.; H; Dolg, M.; Stoll, H.; PreuB, H.*Theor. Chim. Acta.* **1990**, *77*, 123–141.
(29) GaussView, version 3.09; Semichem Inc.: Shawnee Mission, KS, 2003.